Calibration Procedures for a Computational Model of Ductile Fracture

Calibration Procedures for a Computational Model of Ductile Fracture

Z. Xue*[§], M.G. Pontin[#‡], F.W. Zok[#] and J.W. Hutchinson*

[*]School of Engineering and Applied Sciences, Harvard University, Cambridge, MA

[#] Materials Department, University of California, Santa Barbara, CA

[§] Presently at Schlumberger Reservoir Completions, Rosharon, TX

[‡]Presently at Ceradyne, Costa Mesa, CA

Abstract

A recent extension of the Gurson constitutive model of damage and failure of ductile structural alloys accounts for localization and crack formation under shearing as well as tension. When properly calibrated against a basic set of experiments, this model has the potential to predict the emergence and propagation of cracks over a wide range of stress states. This paper addresses procedures for calibrating the damage parameters of the extended constitutive model. The procedures are demonstrated for DH36 steel using data from three tests: (i) tension of a round bar, (ii) mode I cracking in a compact tension specimen, and (iii) shear localization and mode II cracking in a shear-off specimen. The computational model is then used to study the emergence of the cup-cone fracture mode in the neck of a round tensile bar. Ductility of a notched round bar provides additional validation.

Keywords: Ductile fracture; Computational fracture; Shear fracture; Damage parameters

1. Introduction

Progress in computational fracture mechanics has paralleled advances in constitutive models that incorporate damage mechanisms. For many ductile structural alloys the mechanism governing failure is void nucleation, growth and coalescence. The grand challenge for these alloys is the development of a computational capability for predicting localization, crack formation and crack propagation under all states of stress. Capturing both tensile (mode I) and shear (mode II) fractures has been particularly challenging. When properly calibrated for a specific structural alloy, the Gurson model [1] and some of its close relatives, such as the Rousselier model [2], have shown

considerable promise for characterizing mode I crack growth [3-8]. In addition, the models have been used to simulate transitions from mode I crack growth to mixed mode shear cracking in the cup-cone fracture process of round tensile bars [9,10] and in three-dimensional through-cracks in thin plates [11]. Such transition problems are generally more challenging because the constitutive models have not been developed to explicitly address damage under shear dominated conditions.

A recent extension of the Gurson model [12] specifically incorporates damage in shear, adding the flexibility to address shear ruptures as well as tension dominated failures. This extension will be employed here in conjunction with a suite of three tests (round bar tension, mode I compact tension, and mode II shear-off) to calibrate the constitutive parameters for the structural steel, DH36. For verification, the calibrated model is then used to study the failure details of several other problems.

To put the overall objectives of this work into some perspective, it is noted that three parameters are required to calibrate the extended Gurson model: the initial void volume fraction, f_0, a shear damage coefficient, k_ω (defined below) and the finite element size, D. To accurately characterize localization and fracture, D must be on the order of the spacing between the voids that dominate the fracture process, typically from tens to hundreds of microns. With mesh requirements this fine, it is only possible to predict the onset and propagation of cracks in relatively small components or in larger structures where the location of the failure can be anticipated in advance. In contrast, it would not be feasible to employ a fracture model of this type to analyze fractures in large structures where the failure locations cannot be anticipated. Under such circumstances, because the finite element size for a large structure is necessarily orders of magnitude greater than void spacing and often larger than plate thickness, coarser criteria based on a critical effective plastic strain or a through-thickness cohesive zone must be employed. These criteria must also be calibrated for each material, but against tests that make no attempt to resolve the fine scale fracture processes relevant for the present class of models. The two classes of fracture models complement each other. In principle, computations based on a fine scale model could be used to calibrate a coarse scale model.

2. The extended Gurson model

The Gurson model is an isotropic formulation that employs the mean stress, $\sigma_m = \sigma_{kk}/3$, and the effective stress, $\sigma_e \equiv \sqrt{3J_2} = \sqrt{3 s_{ij} s_{ij}/2}$, where $s_{ij} = \sigma_{ij} - \frac{1}{3}\sigma_{kk}\delta_{ij}$ is the stress deviator. The extended model [12] employs, in addition, the third stress invariant

$$J_3 = \det(\mathbf{s}) = \frac{1}{3} s_{ij} s_{ik} s_{jk} = (\sigma_I - \sigma_m)(\sigma_{II} - \sigma_m)(\sigma_{III} - \sigma_m) \tag{1}$$

where the expression on the right is couched in terms of principal stresses, assumed to be ordered as $\sigma_I \geq \sigma_{II} \geq \sigma_{III}$. The non-dimensional metric

$$\omega(\boldsymbol{\sigma}) = 1 - \left(\frac{27 J_3}{2 \sigma_e^{\,3}} \right)^2 \tag{2}$$

lies in the range, $0 \leq \omega \leq 1$, with $\omega = 0$ for all axisymmetric stress states,

$$\sigma_I \geq \sigma_{II} = \sigma_{III} \quad \text{or} \quad \sigma_I = \sigma_{II} \geq \sigma_{III}, \tag{3}$$

and $\omega = 1$ for all states comprised of a pure shear stress plus a hydrostatic contribution,

$$\sigma_I = \tau + \sigma_m,\ \sigma_{II} = \sigma_m,\ \sigma_{III} = -\tau + \sigma_m \qquad (\tau > 0) \tag{4}$$

The original Gurson model was formulated and calibrated based on the mechanics of void growth under axisymmetric stress states. The extension [12] does not alter the model for these states. The extension modifies the predictions for states with non-zero $\omega(\boldsymbol{\sigma})$. In particular, a contribution to damage growth under pure shear stress states is accounted for in the extension whereas the original Gurson model predicts no change in damage for states having $\sigma_m = 0$.

The yield surface of the extended Gurson model is the same as the original. Including the fitting parameters, q_1, q_2 and q_3, introduced by Tvergaard [13], it is given in terms of the effective and mean stress measures by

$$F(\sigma_e, \sigma_m, f) = \left(\frac{\sigma_e}{\sigma_M} \right)^2 + 2 q_1 f \cosh\left(\frac{3 q_2}{2} \frac{\sigma_m}{\sigma_M} \right) - \left(1 + q_3 f^2\right) \tag{5}$$

The current state is characterized by f, the "apparent" void volume fraction, and σ_M, the current effective stress governing flow of the damage-free matrix material. All

quantities not labeled with the subscript *M* represent overall quantities associated with the bulk material. Normality implies that the plastic strain rate, D_{ij}^P, is given by

$$D_{ij}^P = \frac{1}{h} P_{ij} P_{kl} \dot{\sigma}_{kl} \tag{6}$$

where

$$P_{ij} = \frac{\partial F}{\partial \sigma_{ij}} = \frac{3 s_{ij}}{{\sigma_M}^2} + \frac{f q_1 q_2}{\sigma_M} \sinh\left(\frac{3 q_2 \sigma_m}{2 \sigma_M} \right) \delta_{ij} \tag{7}$$

In finite strain formulations, $\dot{\sigma}_{ij}$ is identified with the Jaumann rate of stress. The hardening modulus, h, is identified in the Appendix. If $\sigma_m = 0$, $P_{kk} = 0$ and the rate of plastic volume change vanishes, i.e. $D_{kk}^P = 0$; this feature persists in the extension. In the absence of nucleation, the extension of the Gurson model posits

$$\dot{f} = (1 - f) D_{kk}^p + k_\omega f \omega(\boldsymbol{\sigma}) \frac{s_{ij} D_{ij}^p}{\sigma_e} \tag{8}$$

The first contribution is that incorporated in the original model while the second is the crux of the extension. As previously noted, the modification leaves the constitutive relation unaltered for axisymmetric stress states. In a state of pure shear, however, (8) gives $\dot{f} = k_\omega f \dot{\gamma}^P / \sqrt{3}$, where $\dot{\gamma}^P$ is the plastic shear strain rate and k_ω is the shear damage coefficient, the sole new parameter in the extended model. The inclusion of the second term in (8) rests on the notion that the volume of voids undergoing shear may not increase, but void deformation and reorientation contribute to softening and constitute an effective increase in damage [14-16]. In addition, the second term can model damage generated by the nucleation in shear of tiny secondary voids in void sheets linking larger voids. Thus, in the extension, f is no longer directly tied to the plastic volume change. Instead, it must be regarded either as an effective void volume fraction or simply as a damage parameter, as it is for example when the Gurson model is applied to materials with distinctly non-spherical voids. Further discussion and illustrations of the extension are given in [12], where the emphasis is on its role in shear localization. The remaining equations specifying the entire description of the model are listed in the Appendix. Included is the specification of the widely used technique [13] that accelerates damage

from $f = f_c$ to $f = f_f$, at which point the material element is deleted. Details of the numerical algorithm used to implement the constitutive model in the finite element code ABAQUS Explicit [16] are also presented in the Appendix.

3. Outline of the calibration protocol

The elastic-plastic inputs into the extended Gurson Model are the Young's modulus, E, the Poisson's ratio, ν, and the intrinsic stress-strain response of the damage-free material ($f_0 = 0$). The two damage-related input parameters are the initial effective void volume fraction, f_0, and the shear damage coefficient, k_ω. Additionally, because the constitutive model contains no material length scale, the size of the finite element mesh, D, is calibrated through crack growth predictions, employing well-established procedures [4, 7].

This paper addresses the general task of calibrating the three fracture-related parameters: f_0, k_ω and D. The procedures are demonstrated through experiments and analyses of DH-36 steel (Fig. 1): a high strength alloy commonly used in ship construction. Following extensive prior work on calibration procedures for the standard Gurson model (e.g., [4, 7]), the present study employs data from a mode I fracture test and a round bar tensile test to identify intrinsic uniaxial stress-strain behavior, f_0 and D. Additionally, a shear off test is added to the suite of tests to determine the shear damage coefficient, k_ω. The paper is organized following closely the steps in the calibration protocol:

Section 4: Determination of the intrinsic stress-strain response of the undamaged material from round bar tensile tests and establishing that f_0, k_ω and D have little influence on the plastic response until neck development is quite advanced.

Section 5: Determination of f_0 and D from compact tension mode I fracture tests and establishing that k_ω has little influence on crack growth prediction when the crack is planar.

Section 6: Determination of k_ω using data from shear-off tests and the previously determined f_0 and D.

Section 7: Discussion of the applicability of the calibrated constitutive model to the cup-cone failure mode as one illustration and the ductility of notched round bars as another. Possible variations in the identification protocol for other materials are also discussed.

The three calibration tests were conducted under quasi-static loading, while all simulations were carried out using the dynamic code ABAQUS Explicit. In order to minimize inertial effects and efficiently simulate the quasi-static tests in the explicit code, a preliminary series of calculations with different fixed applied loading rates was performed for each test configuration. At some loading rate, as the rates decrease, the simulations converge to a quasi-static limit. That loading rate was then employed in all subsequent calculations. Material strain-rate dependence is ignored in the present computations.

4. Intrinsic plastic response of the undamaged material

The plastic response of the undamaged material ($f_0 = 0$) was obtained from quasi-static uniaxial tensile tests on round bars coupled with elastic-plastic finite element computations. The test geometry and finite element mesh are shown in Fig. 2. The nominal axial strain ε_N was measured using a non-contacting laser extensometer over a central 12.7 mm length within the gauge section. Prior to necking, the true (logarithmic) strain is given by $\varepsilon_T = \ln\left(1+\varepsilon_N\right)$ and the true stress by $\sigma_T = \sigma_N\left(1+\varepsilon_N\right)$, where σ_N is the nominal stress (load/initial area). To ascertain the true response in the post-necking regime, computations were performed using an assumed form of the stress-strain relation (detailed below) and matching the predicted nominal stress-strain curves with those obtained experimentally. To accurately capture strain localization, a finite strain formulation of elasto-plastic theory was employed in the finite element model. Four-node axisymmetric elements with reduced Gaussian integration (CAX4R in ABAQUS/Explicit [16]) were used. The model was based on an axisymmetric mesh comprised of square section elements with size, $D = 50\mu m$, providing more than 30 elements across the gauge radius. The element size was selected to be consistent with the value emerging from the calibration of the mode I fracture data, presented in the next section. Nevertheless, since

the selected element size is already very much smaller than the macroscopic specimen dimensions and hence the strains are adequately resolved, further reductions in element size would have essentially no effect on the intrinsic (damage-free) stress-strain response. Additional computations were performed to demonstrate that f_0 and k_ω do not affect the identification of the true stress-strain curve even up to strains approaching that for rupture.

The average true stress-strain curve from five tensile tests is plotted in Fig. 3a. This curve was subsequently used to characterize the stress-strain response for stresses below that corresponding to the load maximum, denoted σ_T^{peak}. To extrapolate beyond σ_T^{peak}, a true stress-strain curve of the form $\sigma_T = \sigma_T^{peak}\left(\varepsilon_T / \varepsilon_T^{peak}\right)^N$ was assumed. A preliminary estimate of the strain hardening exponent N was obtained by a least squares fit of the small strain data. A series of finite element computations was then performed to ascertain the full nominal tensile stress-strain curve, using a range of values of N, guided by the preceding curve fitting. As shown in Fig. 3b, the results for $N = 0.185$ (and $f_0 = 0$) accurately replicate the experimental measurements up to the onset of rupture (at a nominal strain of $\varepsilon_N = 0.32$). In summary, the true stress-strain curve used to characterize the damage-free material ($f_0 = 0$) is given by the experimental curve below σ_T^{peak} and the power law extrapolation at stresses above σ_T^{peak}.

For $\varepsilon_N < 0.3$, void growth has almost no effect on the tensile behavior of DH36. This result is demonstrated in Fig. 4 by comparing the experimental data with finite element computations based on a hardening exponent $N = 0.185$ and several representative initial void volume fractions (including the Mises limit, wherein $f_0 = 0$). Other than f_0, k_ω and D, the basic parameters characterizing the constitutive model that are used in all simulations in this paper are:

$$E = 210MPa,\ \nu = 0.3,\ N = 0.185,\ q_1 = 1.5,\ q_2 = 1,\ q_3 = 2.25,$$
$$f_c = 0.15 \text{ and } f_f = 0.25 \qquad (9)$$

The comparisons show that the effects of void growth, manifested in a divergence in the stress-strain response from that of a Mises material, are important only very near the point of final rupture for the DH36 tensile specimen. Their effect is to accelerate the

softening of the material such that the load drops more rapidly than that predicted for the damage-free material. Further details of the failure process in the neck, including formation of a cup-cone fracture surface, are presented in *Section 7*.

5. Determination of f_0 and D from compact tension tests

Compact tension tests were performed on specimens with the geometry shown in Fig. 5a. Crack mouth opening displacement was measured using a non-contacting extensometer and a pair of fiducial tapes mounted on the specimen edge, separated by a distance of 14 mm. Optical images of the broad sample surface were periodically recorded. The experimental measurements and observations are summarized in Figs. 6 and 7. Significant nonlinearity due to plasticity is evident in both the load-displacement response and in the optical images at displacements above $0.5\,mm$. Following an initial rising portion, the load-displacement curve reaches a maximum, at a displacement of about 3–4 mm. This point corresponds to the emergence of a crack on the external surface of the sample (Fig. 7d-f). Further growth both at the surface and in the interior occurs under decreasing load.

The corresponding finite element model is shown in Fig. 5b. In the present analysis, deformations are restricted to be symmetric with respect to the mid-plane such that a symmetry boundary condition is applied to the mid-plane. Consequently, the region meshed is only one half of the full specimen. Eight-node brick elements with reduced Gaussian integration (C3D8R in ABAQUS/Explicit [16]) were used. Iterations on element size and meshing details were made prior to arriving at the mesh used to carry out the final analysis. The smallest elements at the mid-plane in the vicinity of the crack tip have dimensions $30\times30\times50\,\mu m$ with $50\,\mu m$ in the through-thickness direction. Near the surface of the specimen and near the tip the element dimensions are $30\times30\times80\,\mu m$. Approximately 100 elements extend from the mid-plane to the surface in the vicinity of the crack tip. The $30\mu m$ in-plane mesh at the tip allows accurate resolution of the initial tip notch. Further away from the notch tip in the region of crack propagation, the in-plane dimensions of the mesh are approximately $50\times50\,\mu m$. Relatively small differences in results were found from a series of computations with

different meshes with element dimensions in the range from $30\mu m$ to $50\,\mu m$. The mesh in Fig. 5b is regarded as having a nominal (characteristic) size $D = 50\mu m$. In order to improve computational efficiency, only the material in the region of crack propagation, which starts from the notch tip to the left edge of the specimen and has width of 7 mm, was modeled using the extended Gurson model. Outside this region, the specimen was modeled using von Mises plasticity (i.e., $f_0 = 0$ and $k_\omega = 0$).

Load-displacement predictions for four values of f_0 (including $f_0 = 0$) and $k_\omega = 2$ are compared with the experimental results in Fig. 6. Over the range plotted, the load of the damage-free specimen increases monotonically with displacement because there is no damage-induced softening or crack growth. In contrast, the prediction for $f_0 = 0.001$ follows the experimental curve closely for displacements as large as $5mm$. Furthermore, it predicts that cracking initiates at the center of the notch front, at a displacement of about $1mm$. Thereafter, the crack grows deeper into the specimen and spreads laterally from the center (Fig. 7). Upon reaching the free surface, at a displacement of 3.6 mm, the load reaches a maximum and a load fall-off ensues. These results agree well with the experimental measurements. The predictions for the two larger values of f_0 clearly over-predict the effect of damage and cracking at displacements below $5mm$. They are particularly deficient in predicting the displacement at the load maximum.

At displacements above $5mm$, the experimental data fall below the numerical predictions for all three values of f_0. This discrepancy arises for two reasons. The symmetry imposed in the simulation precludes the transition to slant fractures that usually develop as the crack advances and the crack in the test is likely to have departed from the imposed symmetry. In addition, element deletion was used to mimic the crack propagation such that the element is deleted when $f = f_f$. As the crack advances, it encounters larger elements in the mesh and these dissipate more energy prior to failure than the calibrated elements with $D = 50\mu m$. It is indeed observed from Fig. 8 for the case of the crack month opening displacement reaching 8 mm that some of the deleted elements are much larger than $D = 50\mu m$. It remains for the future to verify that

predictions based on the present choices of f_0 and D can replicate the present experimental results for larger displacements using a computational model with no symmetry restrictions, as well as a uniform mesh with the same calibrated element size throughout the region of crack propagation. Unfortunately, this would result in a significant increase in computational size that would not be feasible for the calibration procedure[1].

Although the results in Fig. 6b were computed with $k_\omega = 2$, the shear damage coefficient has essentially no effect on these predictions. To illustrate this, results for $f_0 = 0.001$ computed with k_ω =2, 2.5 and 3 are plotted in Fig. 6a. The response undergoes only very slight softening with increasing k_ω but remains well within the range of the experimental data. The weak dependence on k_ω is consistent with the fact that mode I cracking occurs over the range of load-displacement data used for the fitting.

In summary, based on the agreement between prediction and experiment for displacements below $5\,mm$, the choices $f_0 = 0.001$ with $D \approx 50\mu m$ are made for DH36.

6. Determination of k_ω from a shear-off test

The fixture in Fig. 9 was designed to create a controlled test in which shear localization gives way to mode II fracture [17]. The corresponding load-displacement curve is used to infer the shear damage coefficient, k_ω. In the test, a plate specimen (3mm thick) is clamped between two thick steel platens, each with a through-hole of diameter19.2 mm. Cylindrical steel plungers, 19.05 mm in diameter, are inserted into each of the two holes, leaving a narrow (0.075 mm) radial gap between the plunger surface and the hole. An additional pair of plungers with slightly reduced diameter (to accommodate Teflon bearings) is then inserted into the holes. The four plungers and the test specimen are then clamped together with a single bolt passing through open holes in each of three of the plungers and the test specimen and a threaded hole in the last plunger, as shown in Fig. 9. With one side of the assembly placed on a stiff supporting base, the

[1] More than ten days were required for each calculation based on the current mesh using a personal computer with memory requirements up to 1GB. The trade-off between efficiency and accuracy suggests that the present calibration strategy is a reasonable compromise.

plunger on the opposite side is load axially in compression. The movement of the plungers induces shear deformation within a narrow cylindrical ring in the specimen. Failure starts as shear localizations near the upper and lower surfaces of the plate which subsequently develop into mode II cracks as the deformation progresses into the plate.

The experimental measurements are summarized in Fig. 10. The coordinate axes are the nominal applied shear stress, $\tau \equiv P/(2\pi RH)$ (R being the plunger radius and H the plate thickness) and the normalized displacement, δ / H . The resulting curves exhibit features reminiscent of those obtained in tension tests. That is, the initial linear region gives way to plasticity at a shear stress of $\sigma_O/2 \approx 240$ MPa (σ_O being the tensile yield stress, obtained from Fig. 3). Following a period of strain hardening, the load reaches a peak, at a displacement of $\delta / H \approx 0.3$–0.4, and subsequently diminishes with increasing displacement. Scanning electron micrographs of a cross-section through a test specimen that had been interrupted following loading to a displacement $\delta / H \approx 0.5$ are presented in Fig. 11. They reveal a diffuse damage zone within the region of intense shear as well as well-defined shear cracks emanating from the specimen surface in the vicinity of the plunger periphery.

A detail of the finite element mesh is depicted in the inset of Fig. 9a. Based on the prior calibrations, computations of shear-off employ an initial void fraction $f_0 = 0.001$ and element size $D = 50\mu m$ in the region of shear localization and cracking. As in the compact tension simulations, computational efficiency was enhanced by only employing the extended Gurson model and the smallest elements in the region of shear localization. Outside this region, the plate was modeled using Mises plasticity and represented by a coarser mesh. Boundary conditions were applied such that the bottom of the lower clamping plate, as well as a small section of the upper clamping plate representing the constraining effect of the clamping bolts, were restricted from all rotation and displacement. Contact between the plate and the clamps and punch was enforced with no tangential sliding. Separation was permitted when the normal traction became tensile. The punch and clamps were modeled as being elastic. Four-node axisymmetric elements with reduced Gaussian integration and hourglass control (CAX4R in ABAQUS Explicit [16]) were used for all components.

The results of the simulations are plotted and compared with experimental measurements in Fig. 10. Simulations for the Mises material ($f_0 = 0, k_\omega = 0$) correlate well with the experimental data for small displacements (δ / H <0.15). However, they over-predict the stresses at larger displacements and do not reveal a load maximum. The results for the standard Gurson model ($k_\omega = 0$) yield essentially identical results up to $\delta / H \approx 0.35$, with only small amounts of softening at larger displacements. Among the other simulations, the best fit of the experimental data for displacements $\delta / H < 0.5$ is that with $k_\omega = 2.5$. Fig. 10 gives a clear trend of the sensitivity of the predictions to the shear damage parameter: the erosion of the shear-off load is significantly underestimated if $k_\omega = 1$ and significantly overestimated if $k_\omega = 4$.

Some details of the progression of the shear-off process – at maximum load $\left(\delta / H = 0.32\right)$ and at a point just before entire ligament fracture ($\delta / H = 0.49$) – are shown in Fig. 12. At maximum load, shear localization and fracture has occurred at the top and bottom surfaces of the plate and some damage has occurred across the entire plate thickness. However, the level of damage in the central region is no larger than about $f = 0.005$, well below that at which the shear stress reaches a maximum ($f \approx 0.03$) [12]. The inference is that for DH36 the present test leads to mode II crack propagation emanating from the plate surfaces rather than global (net-section) rupture. In the second case, for $\delta / H = 0.49$, the ring cracks have extended well into the plate interior and the damage parameter in the center has almost reached the failure level, $f \approx f_F = 0.25$. The ligament undergoes complete fracture in the next increment and the load drops abruptly to zero. The final stages of the failure process are not accurately captured because the simulation does not account for friction between contacting crack surfaces. Element deletion also plays a role. In the narrow region of shear-off, the plastic strain and damage is almost uniform before the shear-off fracture occurs. Multiple elements are predicted to fail almost simultaneously predicting of a loss of load carrying capacity that is almost certainly too rapid. Nevertheless, the main features of the initiation of damage growth in shear and its progression to a well-developed mode II

crack in DH36 appear to be well represented by the extended Gurson Model with $k_\omega = 2.5$ when $f_0 = 0.001$ and $D = 50\mu m$.

7. Applications of the computational model

7.1 Cup-cone fracture of a round tensile bar.

In the discussion of Fig. 4 it was noted that damage plays almost no role in the tensile behavior of a round bar of DH36 well beyond the onset of necking. Not until the load has fallen to below 60% of the maximum load does damage have noticeable effect on the overall load-elongation behavior. In this section, the computational model with the calibrated parameter values for DH36 ($f_0 = 0.001$, $k_\omega = 2.5$) is used to analyze the development of damage within the neck and the trajectory of the ensuing macroscopic crack. This provides a further test of the predictive capability of the extended Gurson model. The key feature of interest is the transition from normal to shear fracture that gives rise to a cup-cone appearance.

Details of the fracture surfaces of the round tensile bars are depicted in Fig. 13. In addition to the classical cup-cone shape observed when the specimen is viewed at low magnifications, three other features are evident. (i) The central (cup) region comprises equi-axed ductile dimples associated with the growth and coalescence of voids in mode I. Although a broad distribution of dimple size is apparent, the average value appears to be of the order of 10 μm. This dimension correlates with the spacing between pearlite colonies (Fig. 1) and suggests that the pearlite serves as the principal void nucleating constituent. (ii) The cone region comprises highly-elongated "smeared" dimples, consistent with void coalescence by shear localization. The latter dimples are comparable in size to those in the cup region, suggesting that the same population of void nucleating sites is activated in both failure modes. (iii) In some regions, the cone consists of more than one shear fracture plane. For instance, on the right side of the surface in Fig. 13(a), the transition from cup to cone first occurs by a downward deviation of the mode I crack as it grows radially from the specimen center. It subsequently deviates from this path and adopts an upward shear path, thereby yielding two distinct shear lips. Furthermore, a closer examination of the cup region near the first transition further suggests that analogous processes occur at smaller length scales. That is, the mode I crack first

attempts to deviate onto an upward path (over a distance of about 100 μm) before diving down to form the first dominant shear lip. These deviations in crack path are likely due to the severity of the neck and the corresponding reduction in stress at even short axial distances from the neck plane.

Tvergaard and Needleman [9] carried out the first detailed computational study of the failure mode in the neck of a round tensile bar based on the unmodified Gurson model. Their work demonstrated that a transition from the planar mode I crack nucleated in the center of the neck to a conical mixed mode shear crack can occur for this constitutive model if a sufficiently fine mesh is used and if a relatively large damage level is invoked. These authors took $f_0 = 0$ and assumed that a 4% volume fraction of voids would be nucleated under increasing strain. Thus, the total void volume fraction nucleated in their simulations far exceeds the void fraction considered to be representative for materials such as DH36. The present calculations suggest that, for realistic void volume fractions (of order 10^{-3}), the transition to conical shear cracking does not occur when the unmodified Gurson model is employed. This finding is borne out by an extensive study of fracture modes in round tensile bars and in plane strain specimens by Besson, Steglich and Brocks [10] using several damage-based constitutive models. More recently, Leblond [18] has pursued these issues further by considering the extended Gurson Model with findings similar to those reported below.

Even when shear damage is included ($k_\omega = 2.5$), simulations with a square mesh in the neck ($50 \times 50 \mu m$) do not predict a transition to a conical crack. Reducing the initial element height such that the element aspect ratio at the onset of fracture is approximately unity at the onset of fracture accommodates a mixed mode conical crack propagating at roughly 45^o to the axis of the specimen. Although this modification does not lead to a transition when the initial element width is set at $D = 50 \mu m$, a well-defined cup-and-cone fracture mode is predicted for slightly smaller element widths (Fig. 14). The fracture patterns in Fig. 14 were computed using the mesh just described for deformations restricted to be axisymmetric but with no symmetry imposed with respect to the plane through the center of the neck. The mesh ($40 \times 6 \mu m$) in Fig. 14(c) gives rise to a near-planar crack in the center of the specimen followed by the transition to a conical

crack after a hesitating start in the opposite direction, broadly consistent with the experimental observations.

7.2 Ductility of straight and notched round bars

The standard definition of the ductility of a metal alloy is the logarithmic strain at failure of a round tensile bar as determined by $\varepsilon_f = \ln(A_0 / A)$ with A_0 / A being the ratio of initial to final cross-sectional areas at the neck. The ductility predicted for the round bar of DH35 with $f_0 = 0.001$, $k_\omega = 2.5$ and the $40 \times 6 \mu m$ mesh is $\varepsilon_f = 1.38$. This value is in close agreement with that measured experimentally: $\varepsilon_f = 1.35 \pm 0.04$ (from five specimens). The ductility prediction is not nearly as sensitive to meshing as the prediction of the transition to the slanted fracture path. For example, the ductility predictions for the other meshes in Fig. 13 are $\varepsilon_f = 1.41$ for a), $\varepsilon_f = 1.44$ for b) and $\varepsilon_f = 1.36$ for d). The fact that ductility predictions are less sensitive to meshing details than crack path transition is consistent with the fact that the overall load-elongation behavior is also relatively insensitive to meshing details. This can be seen in Fig. 15 where nominal stress-strain curves are presented corresponding to some of the same meshes used in the mode transition study in Fig. 14. The cross-sectional area of the neck becomes nearly "frozen" as soon as a normal localization band forms in the center of the neck much before the mode transition. Thus, an accurate ductility prediction relies primarily on the ability of the constitutive model to capture the onset of a normal localization since the onset itself is not very sensitive to mesh size, assuming the mesh is adequate to accurately resolve the stresses and strains in the neck.

As a final validation of the calibrated computational model, the ductility of a notched round bar of DH36 has been computed. The specimen geometry and the mesh in the critical region are shown in Fig. 16. The predicted ductility is $\varepsilon_f = 0.98$. By comparison, the experimentally measured values from three test specimens fall in the range $\varepsilon_f = 0.91 - 0.93$. Thus the model correctly predicts the reduction in ductility due to the increased stress triaxiality arising from the notch geometry.

8. Concluding remarks

This paper has demonstrated that, when properly calibrated, the extended Gurson model has considerable promise as a computational tool for predicting the formation of cracks and their subsequent propagation in ductile structural alloys under a wide range of stress states. By incorporating a parameter to characterize damage in shear, the extended model widens the scope of applications to failure modes with a heavy component of shear. The calibration protocol employed here uses three types of tests: (i) uniaxial tension of a round bar, to infer the intrinsic stress-strain behavior of the undamaged material; (ii) mode I cracking in a compact tension specimen, to calibrate the initial void volume fraction and the element size; and (iii) mode II cracking in a newly-designed shear-off test, to determine the shear damage coefficient. For the alloy in the present study, DH36, it was established that these three calibration steps can be conducted independently, assuming that the sequential order listed above is followed. The calibration process might turn out to be more complicated for other materials, e.g., the shear damage coefficient might influence the calibration of the other two parameters in step (ii). It is worth noting that a variation on the procedure employed here in step (ii) would be to choose f_0 and D to fit resistance curve data in the form of the J-integral vs. crack growth, $J_R(\Delta a)$, extracted from a side-grooved compact tension specimen designed to sustain a straight crack front. The work of Xia and Shih [4] reveals that $J_{IC} = C\sigma_Y D$ where C lies in the range from 2 to 5 depending on N and f_0. For DH36 with $N = 0.185$ and $f_0 = 0.001$, $C \cong 5$ such that the formula gives $J_{IC} \cong 120 kJm^{-2}$ with $D = 50\mu m$. This variation based on $J_R(\Delta a)$ has the attraction that the calibration is directly tied to the mode I toughness of the material.

As noted in the Introduction, it is not feasible to use the fine scale computational model developed here for failure analysis of large structures, except possibly when the precise location of the crack path can be anticipated. The element size in the region of fracture for relatively tough structural alloys will be in the range from tens to hundreds of microns. Thus, application of damage models of the present type will usually be restricted to the study of basic aspects of crack formation and to cracking in structural components and in metal forming and joining processes. A method being developed [19]

that is capable of analyzing the failure of large plate and shell structures is the extended finite element method (XFEM) wherein localizations and cracks occur within large elements (compared to plate thickness, for example) and aligned in any direction. In such coarse scale formulations the fracture process is usually represented by a cohesive zone representing the overall traction-separation behavior averaged through the thickness of the plate or shell. The present fine scale computational model can be used to generate the criterion for the propagation direction and the overall traction-separation relation required for implementing the XFEM model.

The extended Gurson model can also be used to study detailed aspects of crack formation and growth as illustrated by the cup-cone failure mode of the round tensile bar. However, to properly capture the transition from mode I to shear cracking, the finite element mesh must be designed to produce elements with nearly unit aspect ratio at failure in the rupture-critical locations. To satisfy this criterion with rectangular elements, the initial element aspect ratio (width to height) must be taken to be about $e^{3\varepsilon_f/2}$. For DH36, with $\varepsilon_f \approx 1.4$, the required aspect ratio is about 8. This value is consistent with that used for the mesh designs that most accurately predicted the transition in failure modes (Figs. 14(c) and (d)). Even more challenging are the three dimensional aspects of the transition of a mode I through-crack in a plate to the mixed mode slant crack that emerges when the crack advance is extensive. As the crack advances, a neck forms ahead of the current crack tip, localizing the plastic deformation and developing into a slanted shear crack in the final stages of separation. As noted in connection with the cup-cone simulations, the prediction of a change in direction of crack path involving a transition from a mode I to a mixed mode separation process is quite sensitive to mesh design [10, 18]. Further effort is needed to create more robust predictive capabilities. A fine scale XFEM formulation using the extended Gurson model to generate the details of the cohesive zone behavior would be worth exploring.

References

[1] Gurson A, Continuum theory of ductile rupture by void nucleation and growth. Part I—Yield criteria and flow rules for porous ductile media. J. Engng Mater Technol 1977; 99: 2-15.

[2] Rousselier G. Ductile fracture models and their potential in local approach of fracture. Nucl Engng Des 1987;105:97–111.

[3] Howard IC, Li ZH, Bilby BA, Ductile crack growth predictions for large center cracked panels by damage modeling using 3-D finite element analysis. Fatigue and Fracture Engng Mater Struct 1994;17: 959–969.

[4] Xia L, Shih CF, Ductile crack growth-I a numerical study using computational cells with microstructurally-based length scales. J Mech Phys Solids 1995; 43: 233-259.

[5] Xia L, Shih CF, Hutchinson JW. A computational approach to ductile crack growth under large scale yielding conditions. J Mech Phys Solids 1995;43(3):389–413.

[6] Steglich D, Brocks W. Micromechanical modelling of damage and fracture of ductile materials. Fatigue Fract Engng Mater Struct 1998;21(10):1175–88.

[7] Gullerud AS, Xiaosheng G, Dodds RH, Haj-Ali R, Simulation of ductile crack growth using computational cells: numerical spects. Engng Fract Mech 2000; 66: 65-92.

[8] Xue L, Wierzbicki T, Ductile fracture initation and propagation modeling using damage plasticity theory. Engng Fract Mech 2008; 75:3276-3293.

[9] Tvergaard V, Needleman A, Analysis of the cup-cone fracture in a round bar tensile bar. Acta metal 1984; 32: 157-169.

[10] Besson J, Steglich D, Brocks W, Modeling of crack growth in round bars and plane strain specimens. Int J Solids Structures 2001; 38:8259-8284.

[11] Bron F, Besson J, Simulation of the ductile tearing for two grades of 2024 aluminum alloy thin sheets. Engng Fract Mech 2006; 73: 1531-1552.

[12] Nahshon K, Hutchinson JW, Modification of the Gurson Model for shear failure. Eur J Mech A/Solids 2008; 27: 1-17.

[13] Tvergaard V, Material failure by void growth to coalescence. Adv Appl Mech 1990; 27: 83-151.

[14] Bao Y, Wierzbicki T, On fracture locus in the equivalent strain and stress triaxiality space. Int J Mech Sci 2004; 46: 81–98.

[15] Barsoum I, Faleskog J, Rupture in combined tension and shear: Experiments. Int. J Sol Struct 2007; 44: 1768–1786.

[16] Tvergaard V, Shear deformation of voids with contact modeled by internal pressure. Int J Mech Sci 2008; 50: 1459-1465.

[17] Nahshon K, Pontin MG, Evans AG, Hutchinson JW, Zok FW, Dynamic shear rupture of plates. J. Mech Mater Struct 2007; 2: 2049-2066.

[18] Leblond J-B, Studies of the cup-cone fracture mode. Work in progress. Private communication . 2009.

[19] Moes N, Dolbow J, Belytschko T, A finite element method for crack growth without remeshing. Int J Numer Meth Engng 1999; 46: 131-150.

[20] Chu CC, Needleman A, Void nucleation in biaxially stretched sheets. J. Engng Mat Tech 1980; 102: 249-256.

[21] Crisfield MA, Non-linear finite element analysis of solids and Structures, Vol.1. West Sussex, UK: Wiley, 1991.

[22] Simo JC, Hughes TJR, Computational inelasticity. New York, USA, Prentice-Hall, 1998.

[23] Belytschko T, Liu WK, Moran B, Nonlinear finite elements for continua and structures. West Sussex, UK: John Wiley and Sons Ltd. 2000.

[24] Ortiz M, Popov EP, Accuracy and stability of integration algorithms for elastoplastic constitutive relations, Int J Numer Methods Engng 1985; 21: 1561-1576.

[25] Aravas N, On the numerical integration of a class of pressure-dependent plasticity models. Int J Numer Meth Engng 1987; 24: 1395-1416.

[26] Nahshon K, Xue Z, A modified Gurson model and its application to punch-out experiments. Engng Fract Mech 2009; 76-8: 997-1009.

Appendix—The remaining equations governing the modified Gurson model and details of the numerical algorithm

The remaining equations governing increments in the modified model are now listed. Void nucleation is not included but it can readily be incorporated [13,20]. The consistency condition for continued plastic loading,

$$\dot{F} = \frac{\partial F}{\partial \sigma_{ij}} \dot{\sigma}_{ij} + \frac{\partial F}{\partial \sigma_M} \dot{\sigma}_M + \frac{\partial F}{\partial f} \dot{f} = 0 , \tag{10}$$

provides the expression for the hardening modulus,

$$h = -\left[\left((1-f) P_{kk} + k_\omega \frac{f \omega}{\sigma_e} P_{ij} s_{ij} \right) \frac{\partial F}{\partial f} + \frac{h_M}{(1-f)\sigma_M} \frac{\partial F}{\partial \sigma_M} P_{ij} \sigma_{ij} \right] \tag{11}$$

Here,

$$\frac{\partial F}{\partial \sigma_M} = -\frac{2\sigma_e^{\,2}}{\sigma_M^{\,3}} + \frac{3 q_1 q_2 f \sigma_m}{\sigma_M^{\,2}} \sinh\left(\frac{3 q_2 \sigma_m}{2\sigma_M} \right) \tag{12}$$

$$\frac{\partial F}{\partial f} = 2 q_1 \cosh\left(\frac{3 q_2 \sigma_m}{2\sigma_M} \right) - 2 q_3 f \tag{13}$$

and h_M is the modulus of the matrix material defined in terms of the logarithmic plastic strain and true stress in uniaxial tension as

$$\frac{1}{h_M} = \frac{d\varepsilon_M^P}{d\sigma_M} \tag{14}$$

The matrix material (i.e. the undamaged material with $f = 0$) is defined by its Young's modulus, E, Poisson's ratio, ν, and relation between logarithmic plastic strain and true stress in uniaxial tension, $\varepsilon_M^P(\sigma_M)$, also considered as the relation between effective plastic strain and effective stress. These are inputs to the modified Gurson Model along with the new parameter k_ω and the initial value of f. As in the original model, plastic work in the matrix is equated to macroscopic plastic work according to

$$(1-f)\sigma_M \dot{\varepsilon}_M^P = \sigma_{ij} D_{ij}^P , \tag{15}$$

such that increments in matrix flow stress can be computed from

$$\dot{\sigma}_M = \frac{h_M \sigma_{ij} D_{ij}^P}{(1-f)\sigma_M} \tag{16}$$

The final step is to identify the stress-rate for finite strain applications and to combine the elastic and plastic strain increments. The stress increments, $\dot{\sigma}_{ij}$, in the above development are identified with objective Jaumann increments, whose Cartesian components coincide with true stress increments for straining in axes parallel to principal stress axes. Void damage diminishes the overall elastic moduli of the material. However,

this is a small effect compared to void influence on plastic behavior and the effect on elasticity is neglected, as usually done in this type of model. Isotropic elastic behavior is assumed. Combining elastic strain rates, D_{ij}^{e}, and plastic strain rates from (6) gives the total strain rate as

$$D_{ij} = M_{ijkl}\dot{\sigma}_{kl} \tag{17}$$

with instantaneous compliances

$$M_{ijkl} = \frac{1+\nu}{2E}\left(\delta_{ik}\delta_{jl} + \delta_{il}\delta_{jk}\right) - \frac{\nu}{E}\delta_{ij}\delta_{kl} + \frac{1}{h}P_{ij}P_{kl}$$

The inverse is

$$\dot{\sigma}_{ij} = L_{ijkl}D_{kl} \tag{18}$$

with instantaneous moduli

$$L_{ijkl} = L_{ijkl}^{e} - \frac{L_{ijmn}^{e}P_{mn}P_{rs}L_{rskl}^{e}}{h + P_{rs}L_{rsmn}^{e}P_{mn}}$$

where the elastic moduli are

$$L_{ijkl}^{e} = \frac{E}{1+\nu}\left[\frac{1}{2}\left(\delta_{ik}\delta_{jl} + \delta_{il}\delta_{jk}\right) + \frac{\nu}{1-2\nu}\delta_{ij}\delta_{kl}\right]$$

Plastic loading has been assumed in writing both (17) and (18); if the increment is elastic, only the elastic moduli and compliances are used. The effective plastic strain-rate is defined in terms of the logarithmic strain rates in the usual way as

$$\dot{\varepsilon}_{e}^{P} = \sqrt{2D_{ij}^{P}D_{ij}^{P}/3} \tag{19}$$

The final failure process beginning with the onset of coalescence and terminated by element deletion is modeled in the manner that has been commonly adopted [13] wherein the growth of the effective void volume fraction is accelerated when $f > f_c$ according to

$$f^{*}(f) = \begin{cases} f, & f \le f_c \\ f_c + \dfrac{1/q_1 - f_c}{f_f - f_c}\left(f - f_c\right) & f_c < f \le f_f \end{cases} \tag{20}$$

As detailed in [13], f is replaced by f^{*} in the yield function (5) and in all the other equations except that $\dot{f}$ in (8) remains unchanged. The material fails when $f = f_f$.

A variety of numerical algorithms for the integration of elastoplastic constitutive equations have been proposed in the literature [21-23]. A class of backward Euler method has proven to lead to accurate and stable results [24] and is now widely used. Aravas [25] established the backward Euler scheme for pressure-dependent plasticity. Within the same framework, the integration algorithm for the present extended Gurson model is derived and briefly described here. Throughout this section, boldface symbols indicate a matrix/vector formulation.

The backward Euler algorithm is based on the following scheme. During the calculations in each time increment, the stresses and state variables are known at the beginning of the increment and their values need to be updated at the end of the increment for given incremental strains $\Delta\boldsymbol{\varepsilon}$. The updated stresses and state variables must satisfy the yield condition, flow rules and evolution laws of the state variables corresponding to the total strains. To do this, the increment is assumed to be purely elastic at the beginning so that the trial stresses are first obtained from the elasticity relation. If the yield function evaluated from the trial stress is greater than zero, a correction procedure is performed to ensure the updated stresses "returning" to the yield surface. In the following, all quantities are evaluated at the end of the increment, unless otherwise indicated.

The elasticity equations give

$$\boldsymbol{\sigma} = \mathbf{C} : \left(\boldsymbol{\varepsilon}^{el} \Big|_t + \Delta\boldsymbol{\varepsilon}^{el} \right) = \boldsymbol{\sigma}^{el} - \mathbf{C} : \Delta\boldsymbol{\varepsilon}^{p} \tag{21}$$

where

$$\boldsymbol{\sigma}^{el} = \mathbf{C} : \left(\boldsymbol{\varepsilon}^{el} \Big|_t + \Delta\boldsymbol{\varepsilon} \right) \tag{22}$$

is the elastic predictor (or trial stress tensor), $\boldsymbol{\varepsilon}^{el}\Big|_t$ is the elastic strain at the start of the time increment and

$$\mathbf{C} = 2G\mathbf{\Pi} + \left(K - \frac{2}{3}G \right) \mathbf{I}\,\mathbf{I} \tag{23}$$

is the linear isotropic elasticity tensor with G and K being the shear and bulk modulus, respectively, and $\mathbf{\Pi}$ and $\mathbf{I}$ being the fourth- and second-order identity tensors,

respectively. Considering the effective stress σ_e and the mean stress σ_m as independent variables, the yield condition (5) is given by

$$F\left(\sigma_e, \sigma_m, f, \varepsilon_M^p\right) = 0 . \tag{24}$$

The flow rule (6) can be rewritten as

$$\Delta\boldsymbol{\varepsilon}^p = \frac{1}{3}\Delta\varepsilon_m \mathbf{I} + \Delta\varepsilon_e \mathbf{n} \tag{25}$$

where

$$\Delta\varepsilon_m = \Delta\lambda\left(\frac{\partial F}{\partial \sigma_m}\right) \tag{26}$$

$$\Delta\varepsilon_e = \Delta\lambda\left(\frac{\partial F}{\partial \sigma_e}\right) \tag{27}$$

$$\mathbf{n} = \frac{3\mathbf{s}}{2\sigma_e} = \frac{3\mathbf{s}^{el}}{2\sigma_e^{el}} \tag{28}$$

with $\mathbf{s}$ and $\mathbf{s}^{el}$ are the stress tensors corresponding to the updated stress tensor $\boldsymbol{\sigma}$ and the trial stress tensor $\boldsymbol{\sigma}^{el}$, respectively. Eliminating the plastic multiplier $\Delta\lambda$ from Eqs. (26) and (27), one obtains an alternative expression of the flow rule,

$$R = \Delta\varepsilon_m \frac{\partial F}{\partial \sigma_e} - \Delta\varepsilon_e \frac{\partial F}{\partial \sigma_m} = 0 \tag{29}$$

In the extended Gurson model, there are two state variables: the equivalent plastic strain in the matrix material, ε_M^p, and the "apparent" void volume fraction f. Substitution of (25) and (28) into (8) gives the evolution law for f as

$$\Delta f = (1 - f)\Delta\varepsilon_m + k_\omega f \omega(\boldsymbol{\sigma})\Delta\varepsilon_e \tag{30}$$

The evolution law for ε_M^p follows from (25), (28) and (15):

$$\Delta\varepsilon_M^p = \frac{\sigma_m \Delta\varepsilon_m + \sigma_e \Delta\varepsilon_e}{(1 - f)\sigma_M} \tag{31}$$

Then (11) can be rewritten using (25) as

$$\boldsymbol{\sigma} = \boldsymbol{\sigma}^{el} - K\Delta\varepsilon_m \mathbf{I} - 2G\Delta\varepsilon_e \mathbf{n} \tag{32}$$

Furthermore, projecting (21) onto $\mathbf{I}$ and $\mathbf{n}$, one obtains

$$\sigma_m = \sigma_m^{el} - K\Delta\varepsilon_m \tag{33}$$

$$\sigma_e = \sigma_e^{el} - 3G\Delta\varepsilon_e \tag{34}$$

In general, solving the above set of nonlinear equations for the six unknowns: σ_m, σ_e, $\Delta\varepsilon_m$, $\Delta\varepsilon_e$, $\Delta\varepsilon_M^p$, Δf completes the integration algorithm. More efficiently, equations (24) and (29) are regarded as the basic equations with $\Delta\varepsilon_m$ and $\Delta\varepsilon_e$ as the primary unknowns to be solved using Newton's method. With z_m, and z_e as the corrections for $\Delta\varepsilon_m$ and $\Delta\varepsilon_e$, the Newton method requires

$$\begin{cases} K_{11}z_m + K_{12}z_e = -R \\ K_{21}z_m + K_{22}z_e = -F \end{cases} \tag{35}$$

where the coefficients K_{11}, K_{12}, K_{21} and K_{22} are readily obtained.

The values of $\Delta\varepsilon_m$ and $\Delta\varepsilon_e$ are then updated:

$$\begin{aligned} \Delta\varepsilon_m &\to \Delta\varepsilon_m + z_m \\ \Delta\varepsilon_e &\to \Delta\varepsilon_e + z_e \end{aligned} \tag{36}$$

and the values of σ_m, σ_e, $\Delta\varepsilon_M^p$, Δf are determined from (33), (34), (30) and (31), respectively. The iterative loop is continued until $\Delta\varepsilon_m$ and $\Delta\varepsilon_e$ converge.

An alternative integration method recently developed in [26] employed all six stress components as independent variables to solved simultaneously using Newton's method. In contrast, the algorithm described here deals with only two independent variables and is more efficient. The present algorithm was implemented into ABAQUS/Explicit [16] through its user material subroutine interface (VUMAT). Several benchmark tests described in [M7] have been performed to verify the code.

Acknowledgment: This work was supported in part by an ONR MURI through grants to the School of Engineering and Applied Sciences at Harvard University and the Materials Department at the University of California, Santa Barbara.

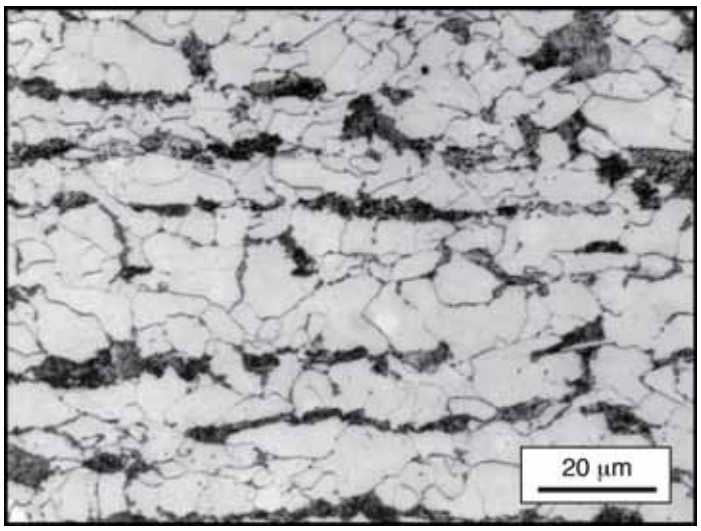

Fig. 1 Optical micrograph of polished and etched cross-section through DH-36 steel plate, showing a microstructure of ferrite (light) and pearlite (dark).

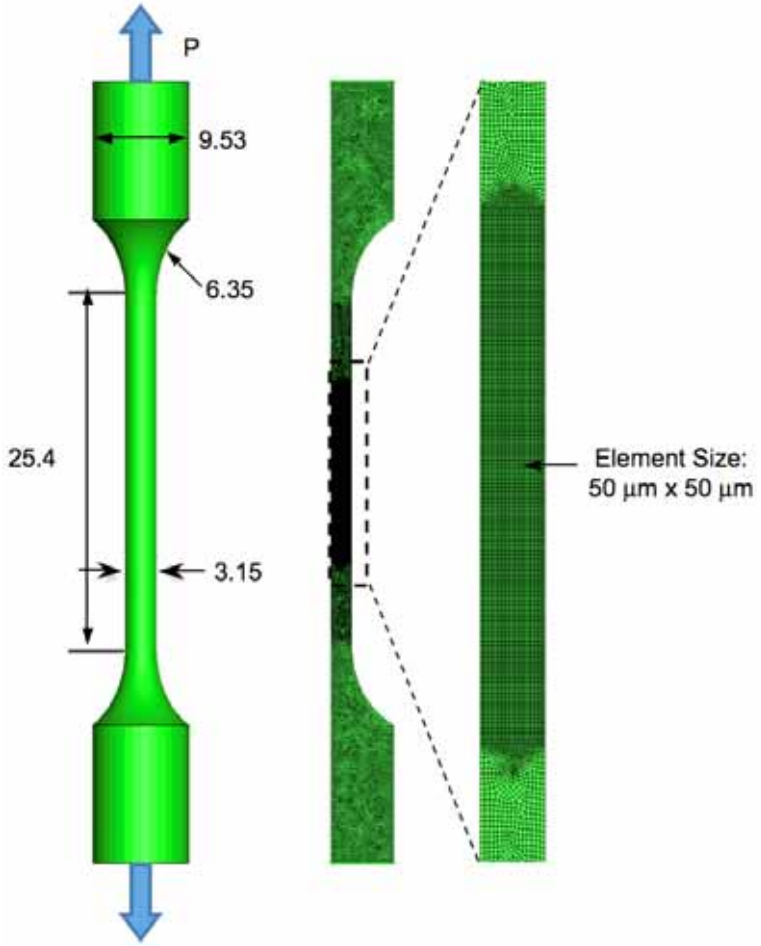

Fig. 2. Tensile specimen geometry and finite element mesh. (Dimensions in mm.)

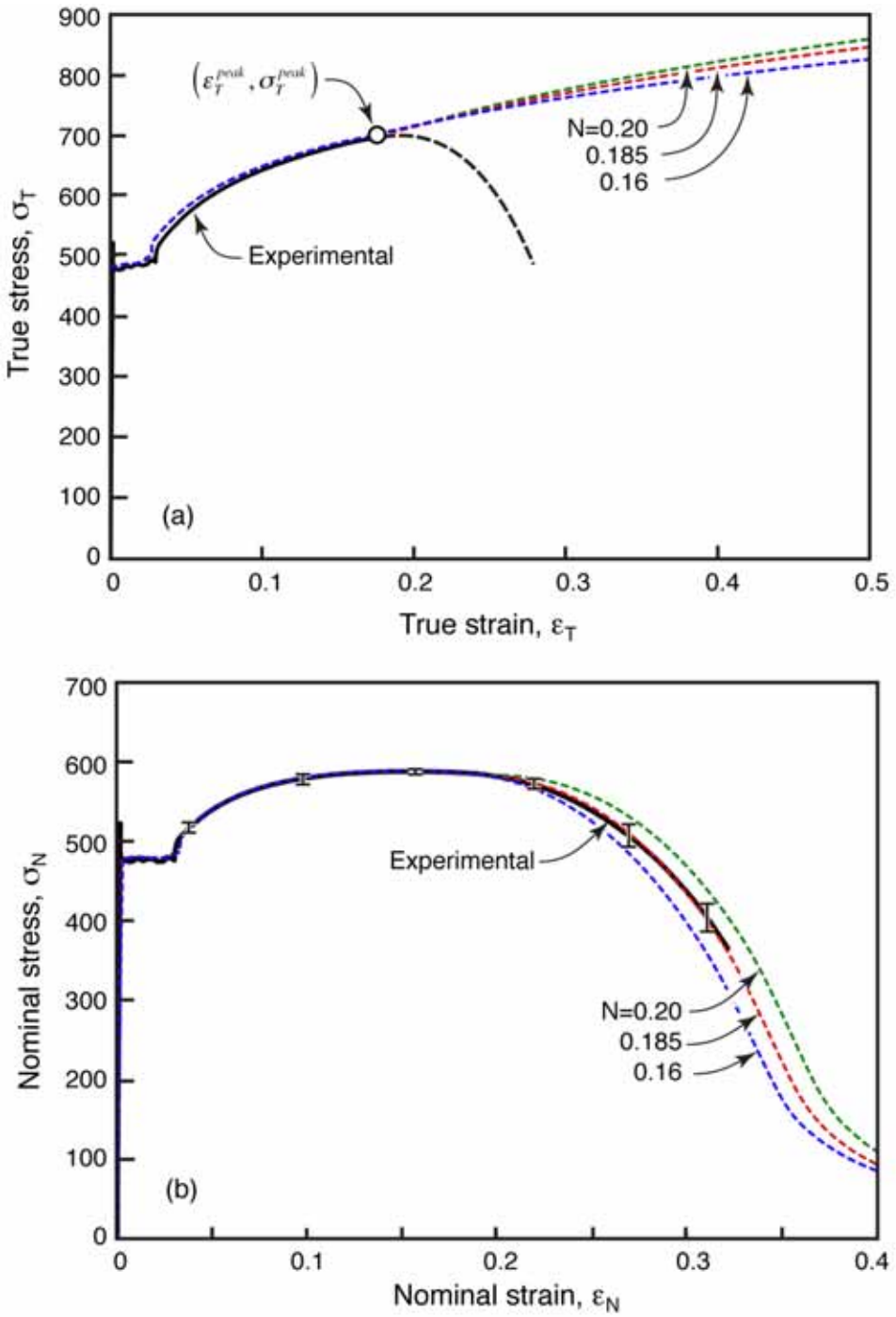

Fig. 3. (a) Power law extrapolation of the true tensile stress-strain curve beyond the onset of necking and (b) the corresponding nominal stress-strain response obtained from finite element analysis. Error bars represent the full range of experimental measurements from six tests. Strain measurements were made using a non-contacting extensometer over a 12.7mm gauge length near the specimen center. The nominal strain, defined as the extension divided by the extensometer gauge length, was consistently employed in both the experiments and the finite element calculations. The tests were performed at a nominal strain rate of 10^{-3} s^{-1}.

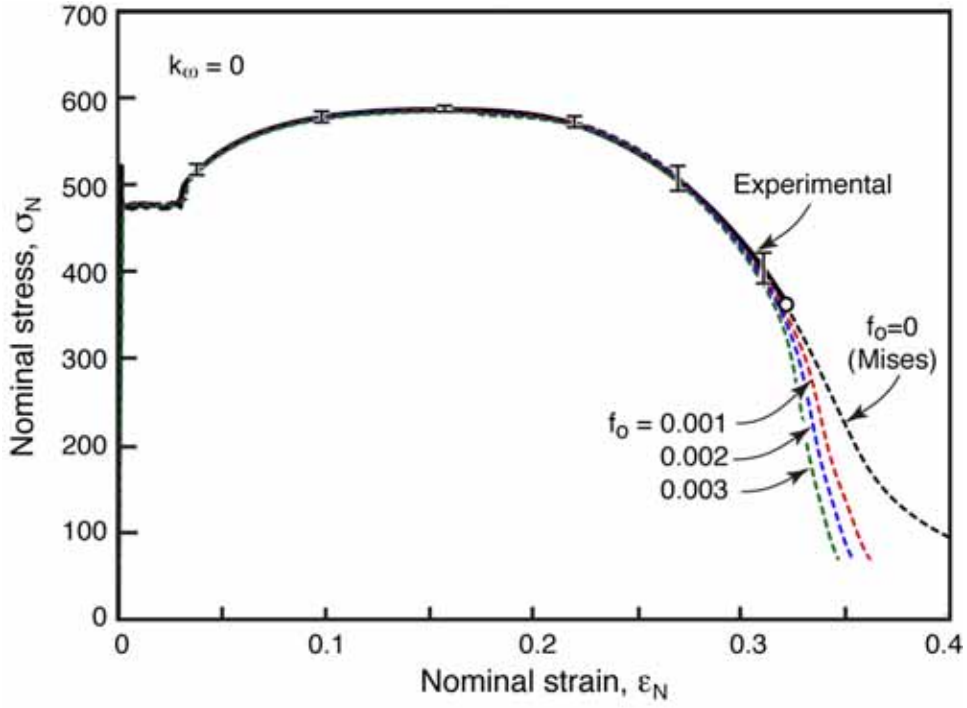

Fig. 4. Effects of initial void volume fraction f_o on the computed nominal tensile stress-strain response. Over the pertinent range of f_o, the computed results are indistinguishable from the experimental measurements up to the point of final fracture.

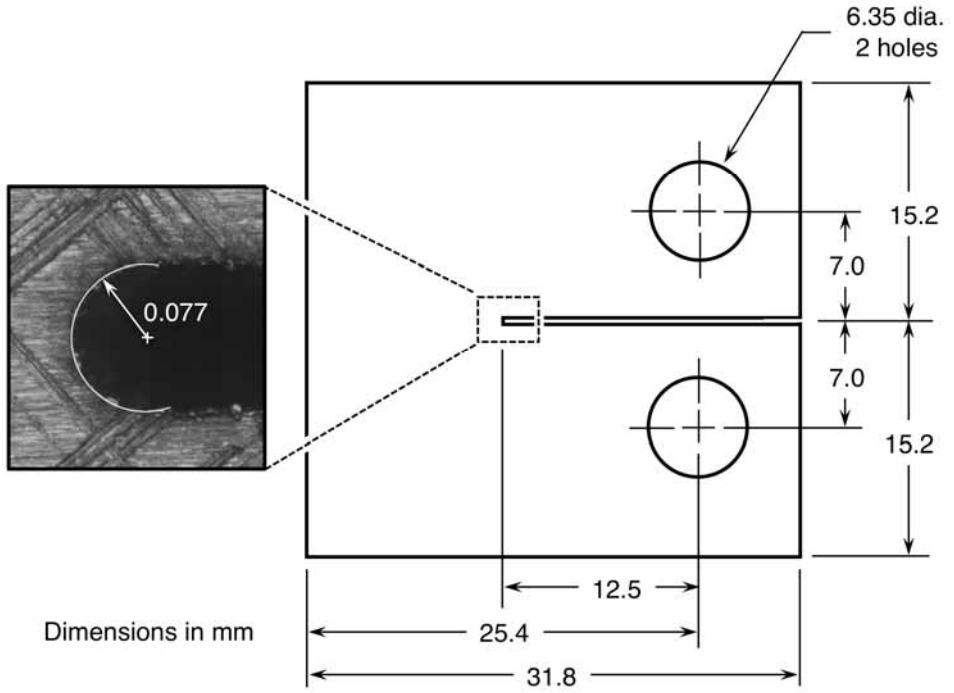

(a)

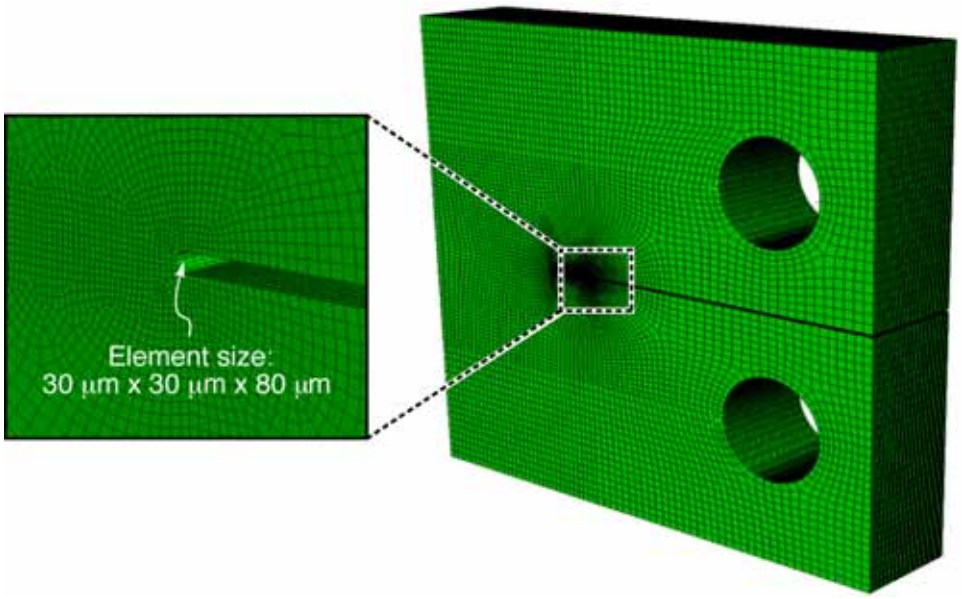

(b)

Fig. 5. (a) Compact tension test geometry employed in the experimental study and (b) corresponding finite element model. Specimen thickness is 12.5 mm. Crack mouth opening displacements were measured using a non-contacting extensometer and a pair of fiducial tapes mounted on the specimen edge, separated by a distance of 14 mm. The same definition was used in the subsequent finite element calculations.

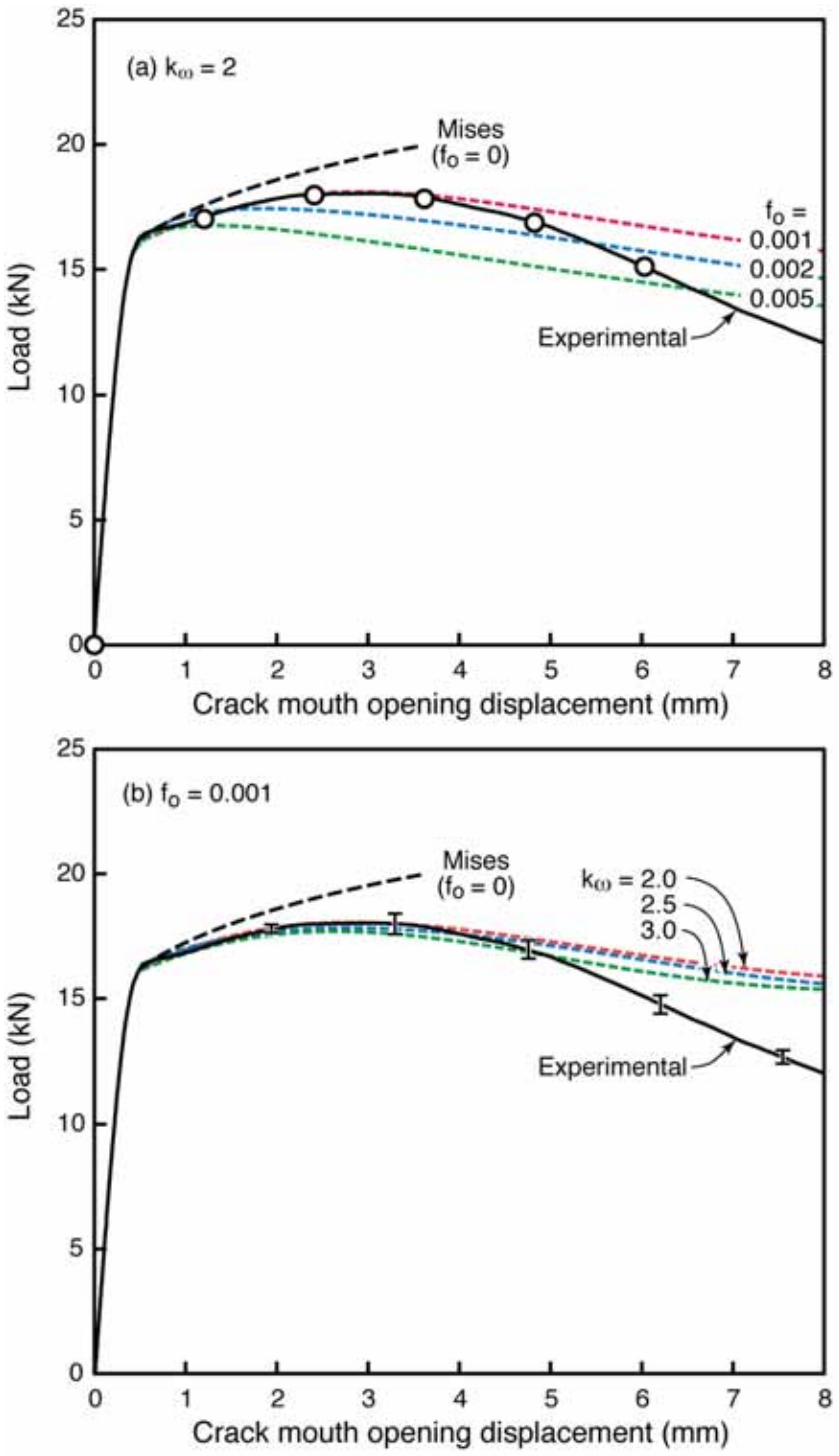

Fig. 6. Effects of (a) f_o and (b) k_ω on the load–displacement response of compact tension tests. Error bars represent the full range of experimental measurements from five tests. Tests were performed at a displacement rate of 1.2 mm/min. Open circles in (a) correspond to images in Fig. 7.

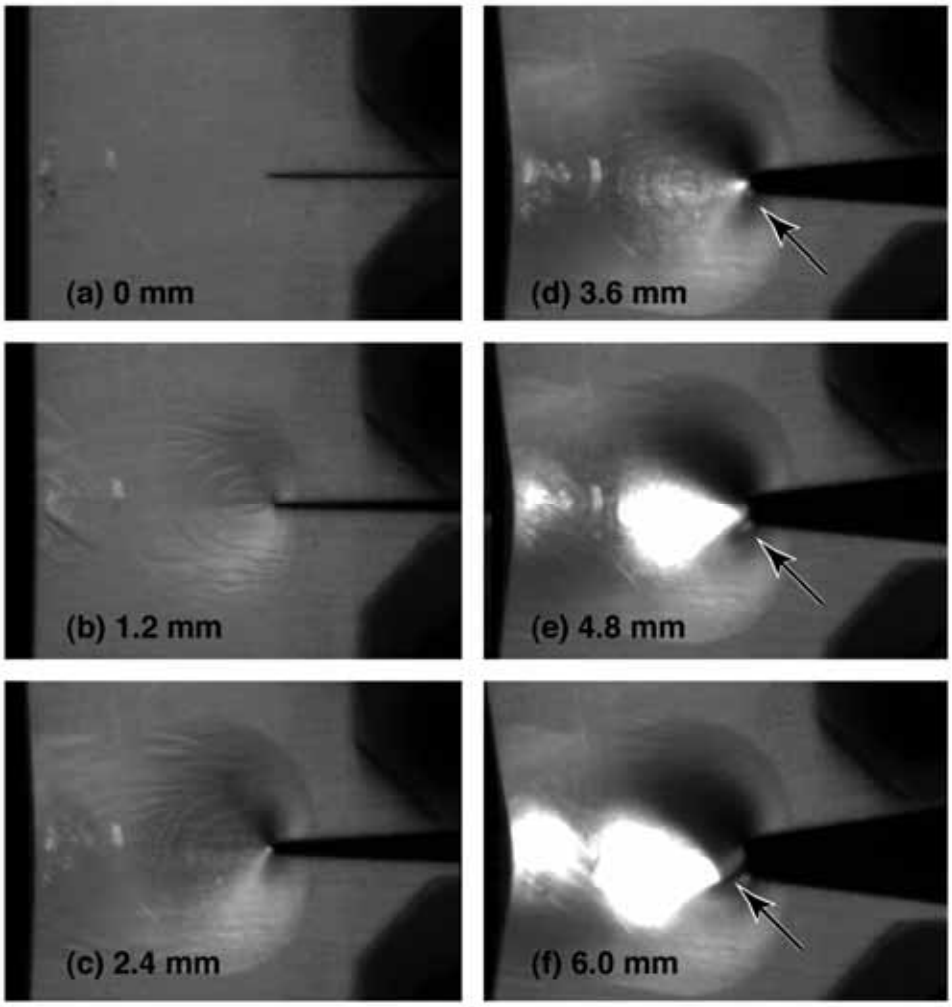

Fig. 7 Images of broad face of compact tension specimen with increasing crack mouth opening displacements. Arrows in the right column indicate the emerging near-surface crack.

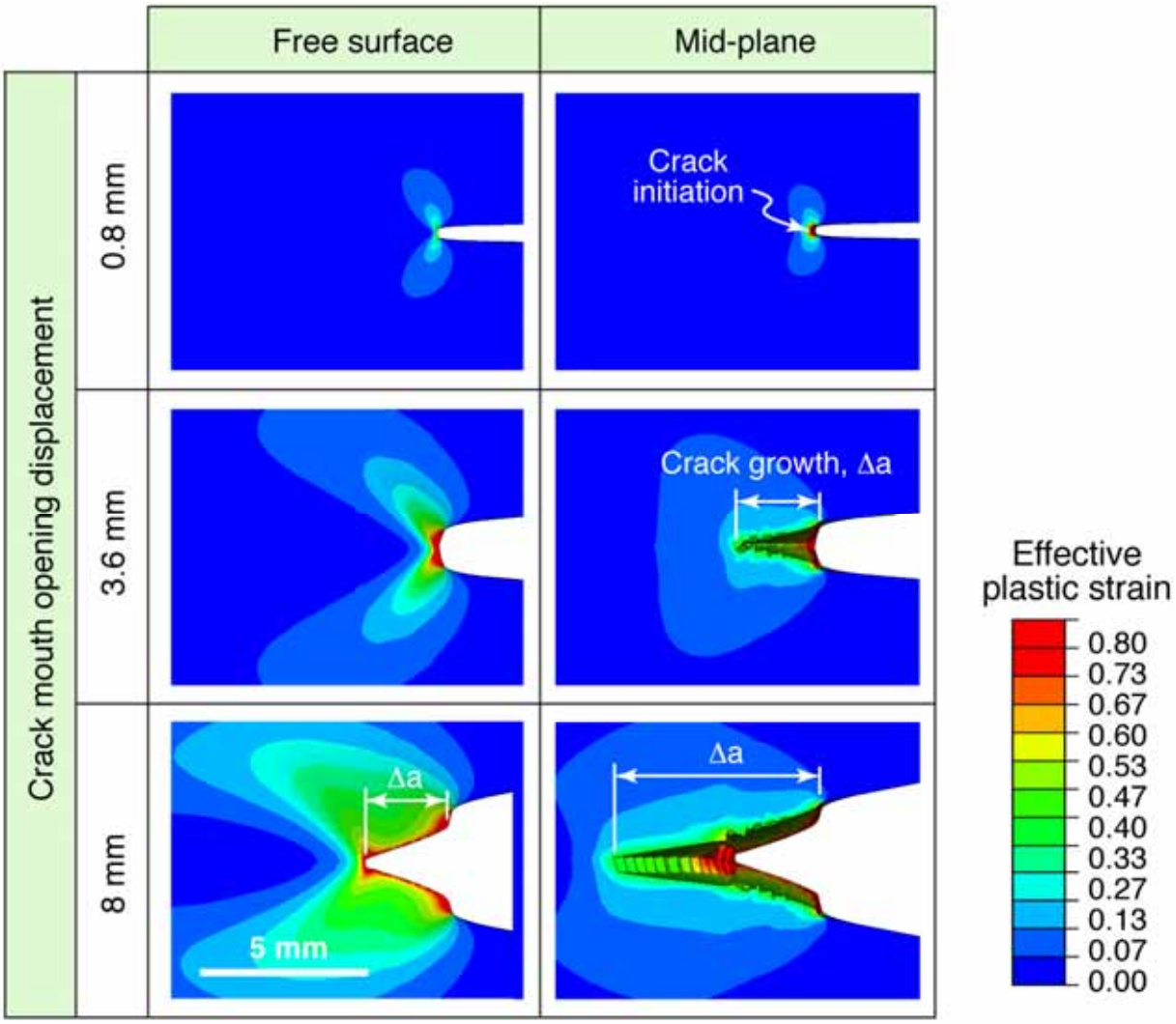

Fig. 8 Evolution of plastic strain and crack growth from finite element calculations of the compact tension test.

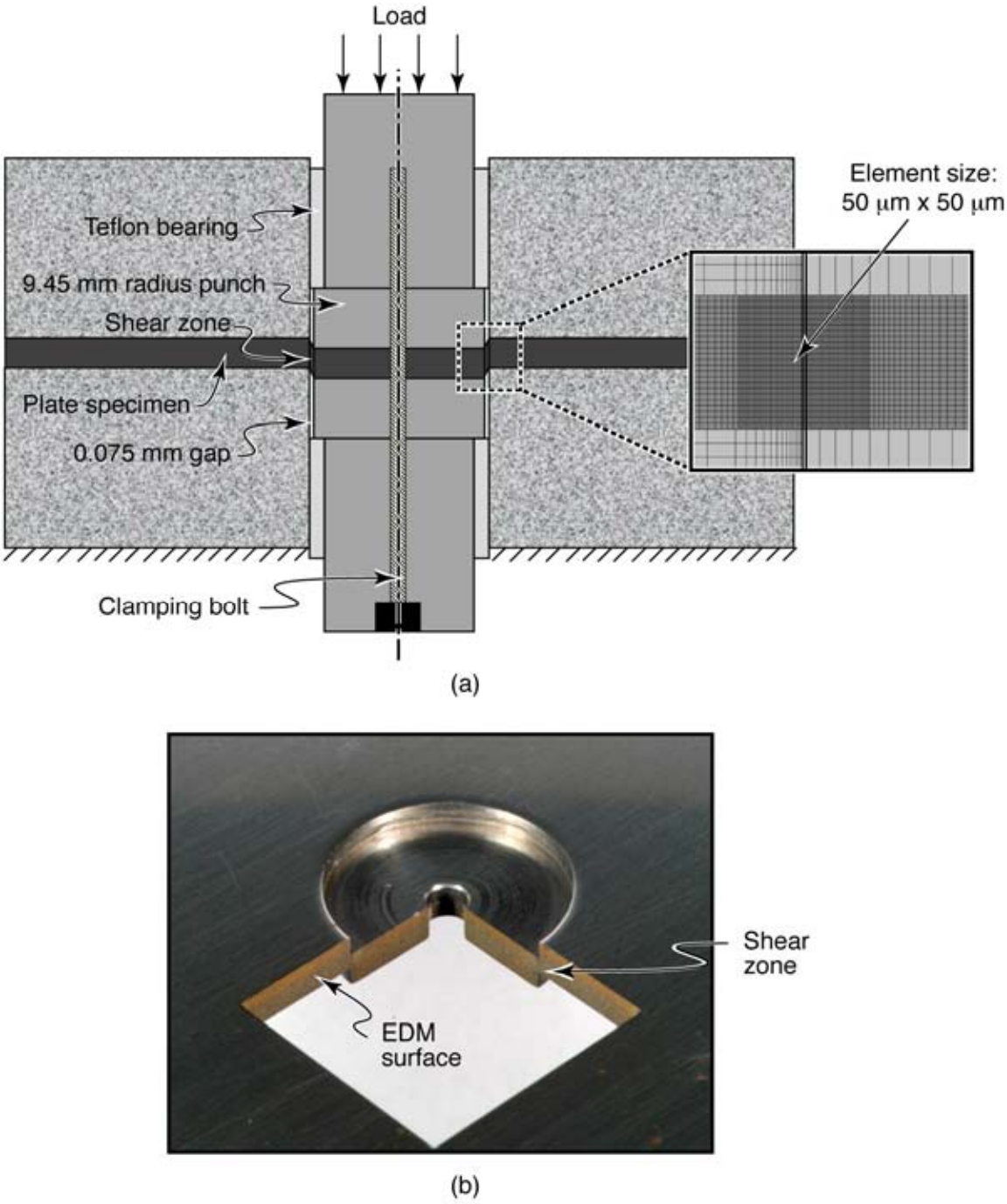

Fig. 9 (a) Shear-off test assembly and detail of finite element model in the region of intense plastic deformation. (b) Macrophotograph of specimen interrupted during shear-off test and sectioned by electrodischarge machining (EDM).

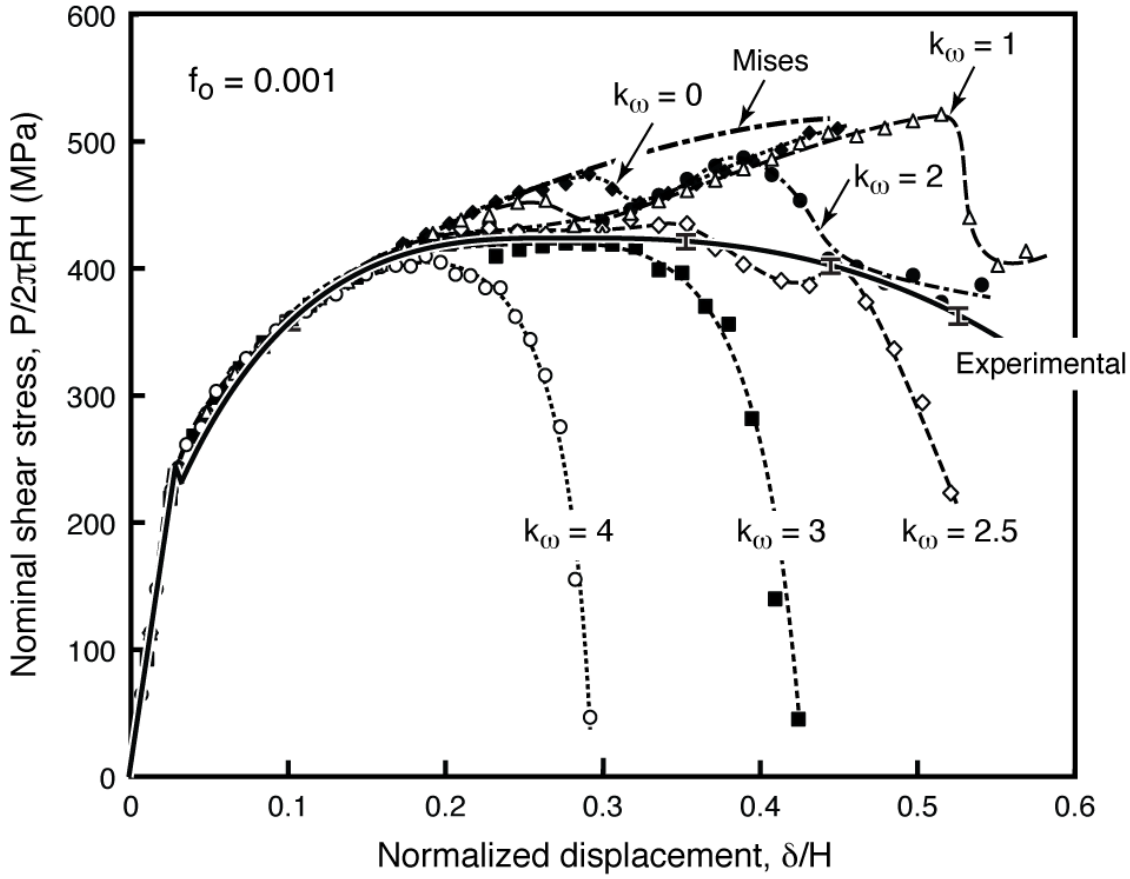

Fig. 10 Measured and computed shear-off response.

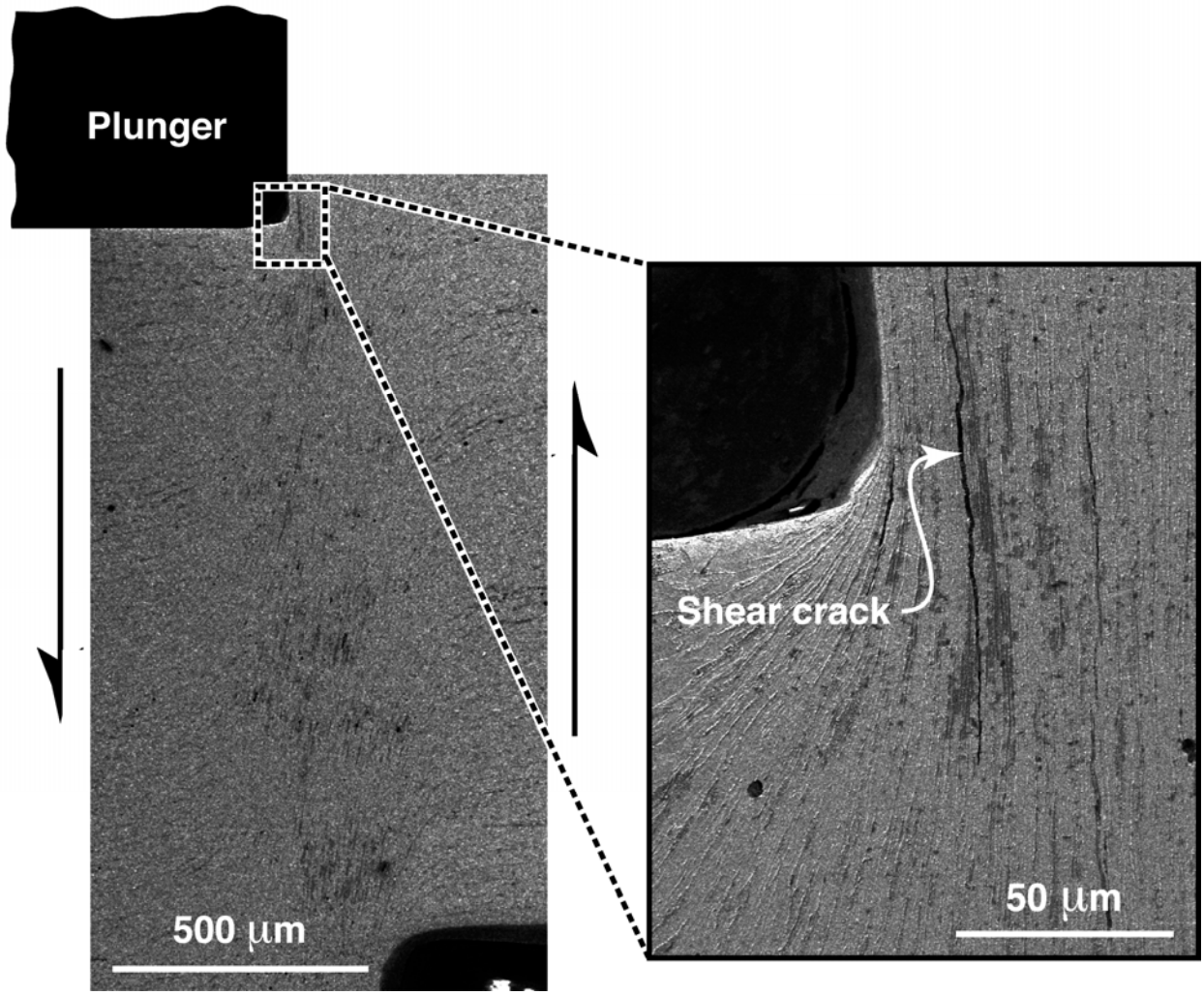

Fig. 11 Scanning electron micrographs of polished cross-sections through shear-off specimen, interrupted at displacement δ/H=0.5.

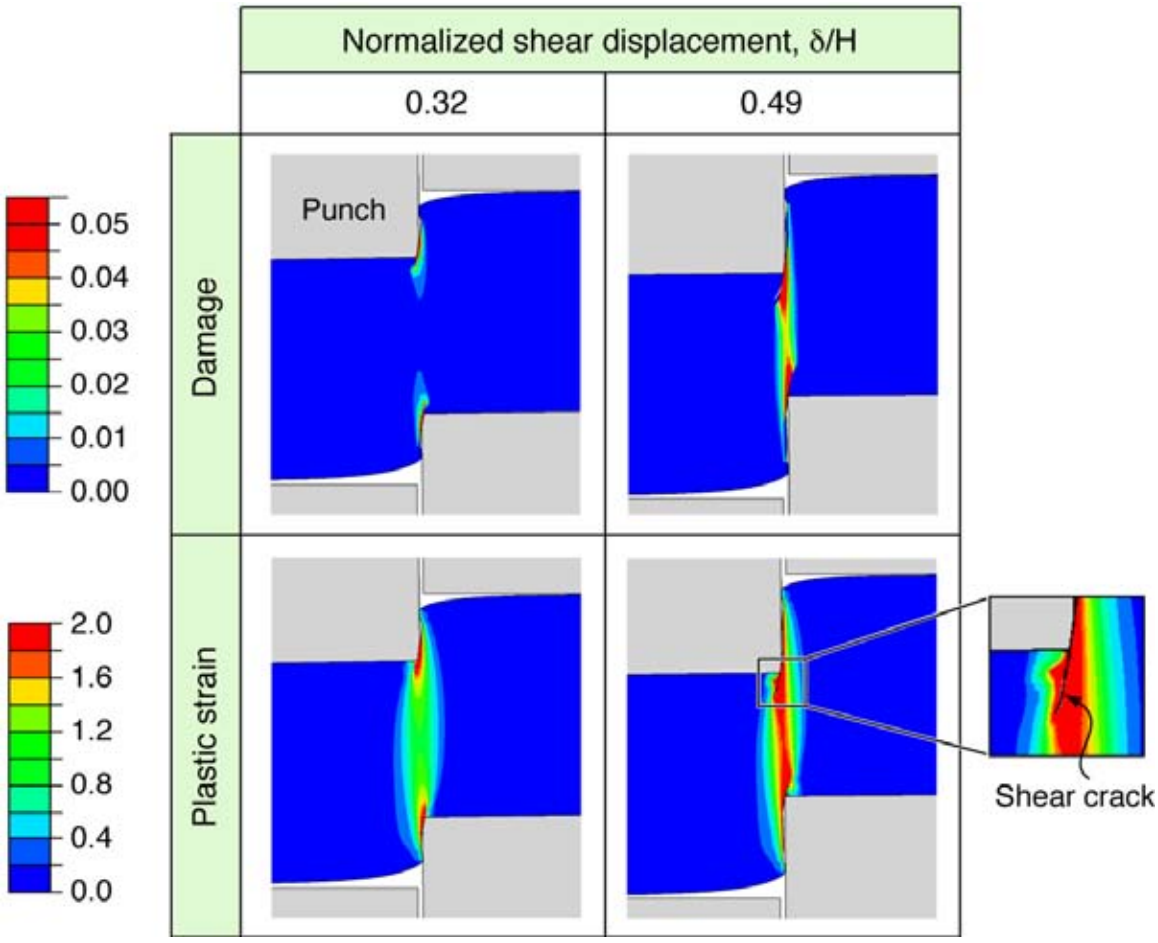

Fig. 12 Evolution of plastic strain and damage from finite element calculations of a shear-off test. Inset (right) shows a shear crack developed in the vicinity of the edge of the contacting punch.

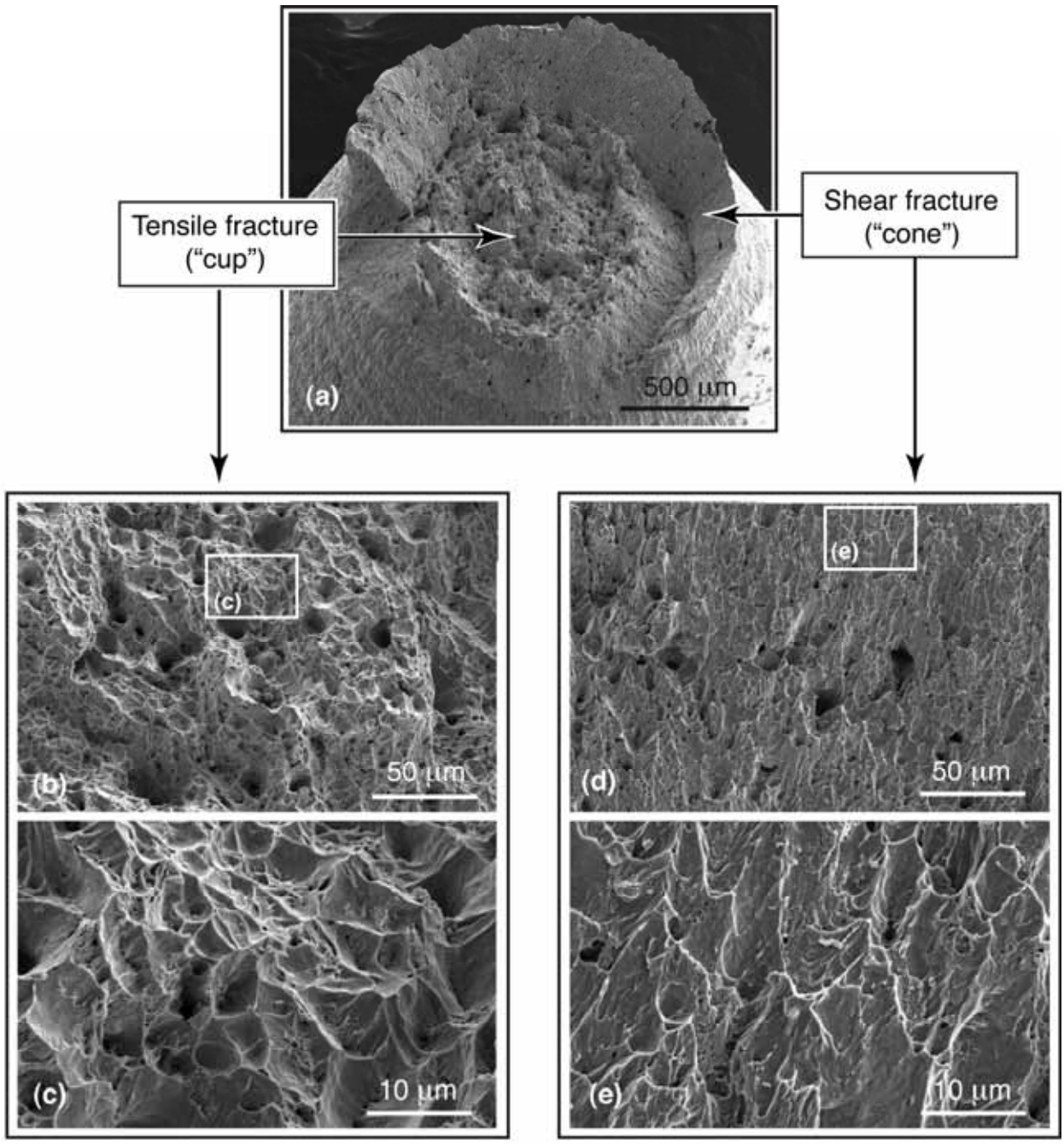

Fig. 13 Fracture surface of DH-36 tensile bar showing: (a) cup-cone failure mode; (b, c) equiaxed dimples caused by void growth and coalescence in the central region; and (c, d) elongated dimples formed by void coalesence during shear lip formation.

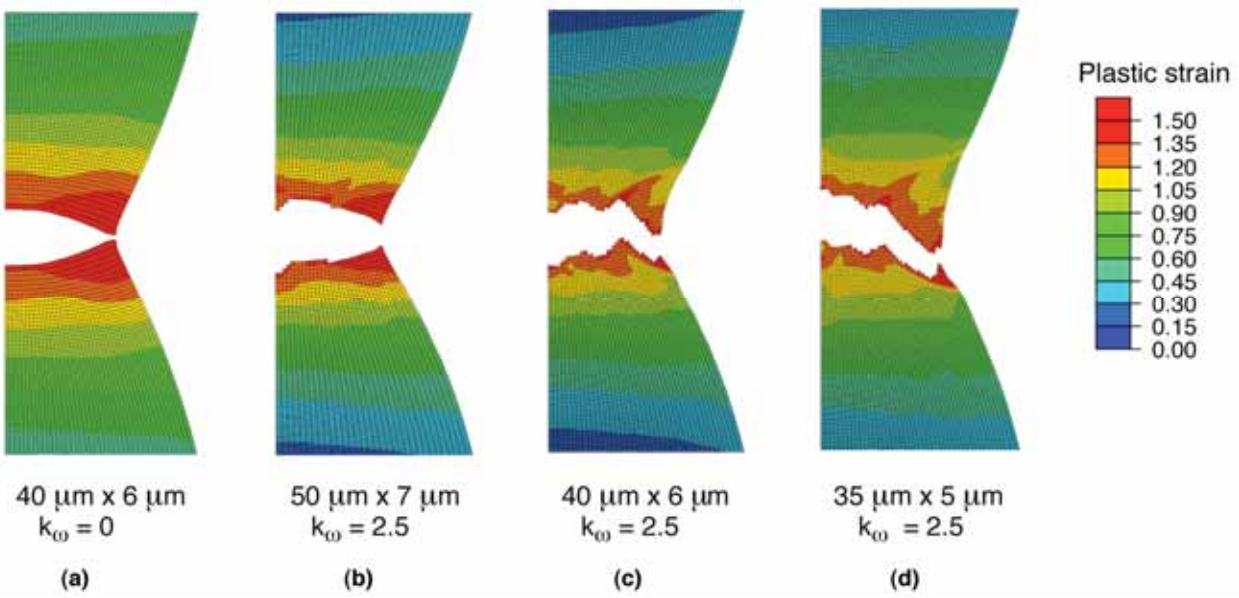

Fig. 14 Effects of initial element size and k_ω on the crack trajectory in an initially unnotched round tensile bar.

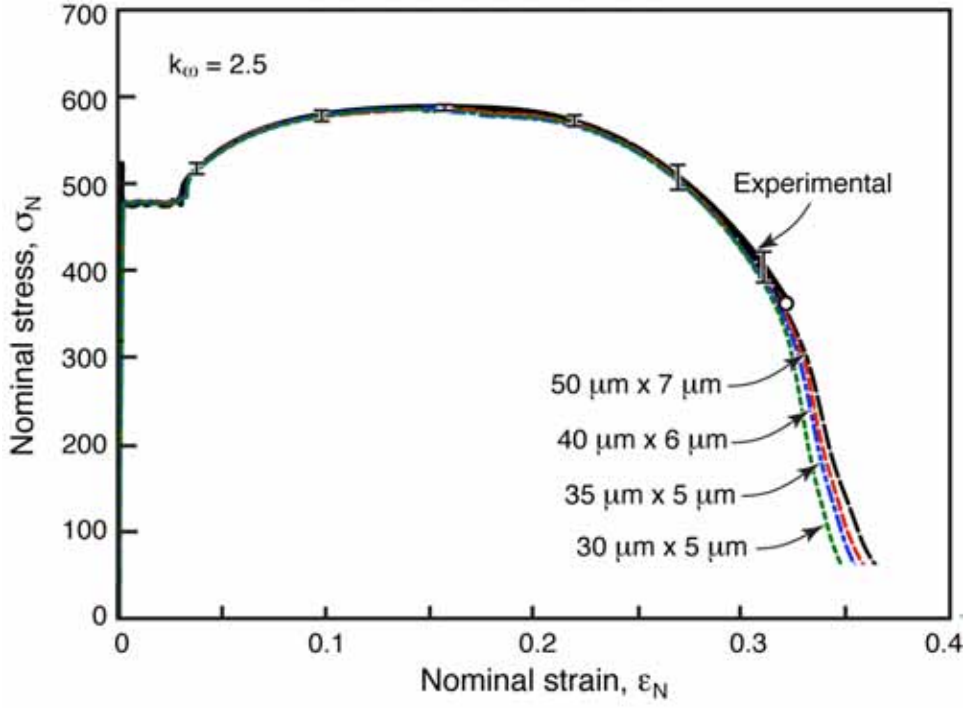

Fig. 15 Effects of initial element size on the computed tensile stress-strain curve.

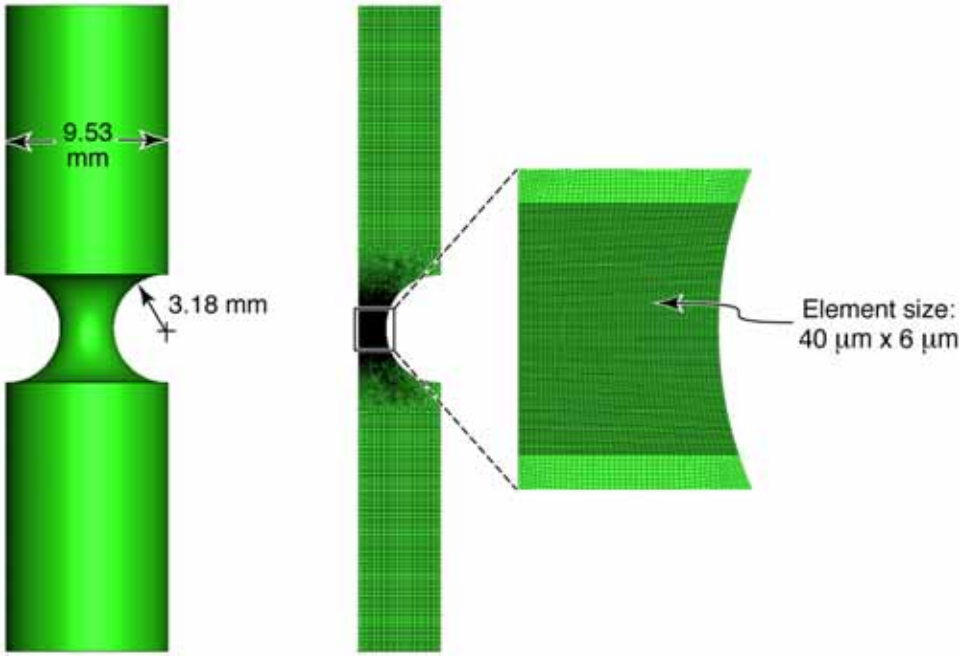

Fig. 16 Notched tensile geometry and corresponding finite element mesh.